The EMERALD Model for the Estimation of the Radial Diffusion Coefficients in the Outer Belt

S Aminalragia-giamini, C. Katsavrias, C. Papadimitriou, I A Daglis, A. Nasi, A. Brunet, S. Bourdarie, N. Dahmen, G. Balasis

AGU ADVANCING EARTH AND SPACE SCIENCE

Space Weather®

RESEARCH ARTICLE
10.1029/2022SW003283

Key Points:

- A machine learning model is developed to derive D_{LL} for the outer radiation belt
- The model uses solar wind parameters as input and can output estimations for user-defined L* values
- The model's accuracy is demonstrated to be high and to outperform established semi-empirical models

Supporting Information:

Supporting Information may be found in the online version of this article.

Correspondence to:

S. Aminalragia-Giamini,
sagiamini@gmail.com;
sagiamini@sparc.gr

Citation:

Aminalragia-Giamini, S., Katsavrias, C., Papadimitriou, C., Daglis, I. A., Nasi, A., Brunet, A., et al. (2023). The EMERALD model for the estimation of the radial diffusion coefficients in the outer belt. *Space Weather*, *21*, e2022SW003283. https://doi.org/10.1029/2022SW003283

Received 8 SEP 2022
Accepted 22 NOV 2022

The EMERALD Model for the Estimation of the Radial Diffusion Coefficients in the Outer Belt

S. Aminalragia-Giamini[1,2], C. Katsavrias[1], C. Papadimitriou[1,2], I. A. Daglis[1,3], A. Nasi[1], A. Brunet[4], S. Bourdarie[4], N. Dahmen[4], and G. Balasis[5]

[1]Department of Physics, National and Kapodistrian University of Athens, Athens, Greece, [2]Space Applications and Research Consultancy (SPARC), Athens, Greece, [3]Hellenic Space Center, Athens, Greece, [4]Department of Space Environment, ONERA, Toulouse, France, [5]IAASARS, National Observatory of Athens, Athens, Greece

Abstract Radial diffusion is one of the dominant physical mechanisms driving acceleration and loss of electrons in the outer radiation belt. Therefore, the accurate estimation of radial diffusion coefficients (D_{LL}) is crucial for detailed radiation belt modeling. In recent years several semi-empirical (SE) models have been developed for the estimation of radial diffusion coefficients which predominantly rely on parameterizations of the Kp index. However, several studies have suggested that the estimations derived from such models can have large deviations from actual (measurement derived) D_{LL} values. In this work we have used the extensive D_{LL} database created in the framework of the Horizon 2020 SafeSpace project which spans 9 years of hourly D_{LL} calculations to develop a model which uses solely solar wind parameters for the derivation of D_{LL} values. The Electric and MagnEtic RAdiaL Diffusion (EMERALD) model is able to derive simultaneously the magnetic and electric components (D^{B}_{LL} and D^{E}_{LL}, respectively) of the radial diffusion coefficient, and furthermore, provide realistic confidence levels on their estimation, which allows the transition from a deterministic paradigm to a robust probabilistic one. Evaluations on the performance of the EMERALD model are shown by comparing its outputs to the D_{LL} data, and examining the reproduction of various D_{LL} characteristics. Finally, comparisons with widely used SE models are shown and discussed.

Plain Language Summary The Earth's outer radiation belt consists of high energy electrons which are characterized by intense variability during solar eruptions and geomagnetic storms. These high energy electrons can cause moderate or severe damage to satellite electronics, therefore the accurate forecasting of their variability is of outmost importance. Radial diffusion, which is quantified by the radial diffusion coefficients, has been established as one of the key mechanisms for the prediction of the electron variability. In this work, we present a new machine learning model for the estimation of the radial diffusion coefficients. The model's accuracy is demonstrated to be high and to outperform empirical forms which are currently used.

1. Introduction

The Earth's outer radiation belt consists of trapped electrons in a broad energy range, from a few hundreds of keV to several MeV. Especially the MeV component of this population is known to present hazards to spacecraft, as these electrons can penetrate through satellite shielding potentially causing internal charging, leading to satellite loss in extreme cases. The dynamics of the electron population are driven by a complex interplay between acceleration and loss mechanisms (Daglis et al., 2019; Reeves & Daglis, 2016). One of the fundamental mechanisms that contributes to the dynamics of the outer belt is radial diffusion, as it can lead to both energization (Jaynes et al., 2018; Katsavrias, Daglis, Li, et al., 2015; Katsavrias, Sandberg, et al., 2019; Nasi et al., 2020, 2022) and loss of relativistic electrons (Katsavrias, Daglis, Turner, et al., 2015; Katsavrias, Daglis, & Li, 2019; Morley et al., 2010; Olifer et al., 2021; Turner et al., 2012). Radial diffusion is frequently juxtaposed to local acceleration when assessing the dominant acceleration mechanism (e.g., Allison and Shprits, 2020). Nevertheless, its importance in the accurate modeling of radiation belt dynamics has been well established (Li et al., 2016; Ma et al., 2016; Shprits et al., 2022).

Radial diffusion is a statistical description, often described as a stochastic process that results in the cross drift shell motion of particles through violation of their third adiabatic invariant via interactions with Pc4-5 ULF waves (roughly in the 2–22 mHz frequency range). The time evolution of the particles due to radial diffusion is described by the 1-D Fokker-Planck equation, which in its simplest form is given by Equation 1:

$$\frac{\partial f}{\partial t} = L^2 \frac{\partial}{\partial L}\left(\frac{D_{LL}}{L^2}\frac{\partial f}{\partial L}\right) \quad (1)$$

where f is the particles' phase space density (PSD), L is Roederer's L* and D_{LL} is the radial diffusion coefficient, which represents the mean square change of L* for a large number of particles over time. The D_{LL} is one of the core inputs of the many physics-based models, which attempt to tackle the kinetic problem of the flow of charged particles within the confines of the Earth's magnetosphere, for example, ONERA's Salammbo model (Beutier & Boscher, 1995; Varotsou et al., 2005, 2008), the Versatile Electron Radiation Belt (VERB) code Subbotin and Shprits (2009), the British Antarctic Survey radiation belt model (BAS-RBM) (Glauert et al., 2014) and the 3-D radiation belt model by Ma et al. (2015, 2018).

Currently, there are two widely used formalisms employed in order to calculate radial diffusion coefficients, that of Fälthammar (1965) and that of Fei et al. (2006). Both approaches require detailed knowledge of the ULF wave power spectral density and, consequently, accurate magnetic and electric field measurements, which of course are not always available. Therefore, efforts have been devoted to describe empirical formulas for the radial diffusion coefficient where such parameterizations are typically based on the Kp index and the L* parameter, for example, Brautigam and Albert (2000), Ozeke et al. (2014), Liu et al. (2016), Ali et al. (2016) and Boscher et al. (2018). Nevertheless, it has been recently shown that such Kp-parameterized D_{LL} can significantly deviate from D_{LL} values calculated from electric and magnetic field measurements, especially during active conditions (Katsavrias et al., 2022; Sandhu et al., 2021).

Efforts have also been devoted in the estimation of D_{LL} for event-specific cases based on sophisticated physics modeling. However, this requires full simulations of the radiation belts over timespans of the order of days which can be unpractical to be run in real-time, and in addition are often found to underestimate the observed magnetic and electric fields which are used in the derivation of D_{LL} (see e.g., the discussion in Tu et al. (2012)). Finally, recently Sarma et al. (2020) developed a probabilistic approach by inferring the values of the radial diffusion coefficients and the loss term parameters, along with their uncertainty, in a Bayesian framework, while Camporeale et al. (2022) used machine-learning methods and specifically Physics-Informed Neural Networks (NNs) to derive a parameterization for D_{LL} at a specific value of the first adiabatic invariant μ as a fixed function of L-shell.

In this work, we present a method for the estimation of radial diffusion coefficients solely from solar wind (SW) characteristics; specifically, SW speed, SW density and the magnitude of the interplanetary magnetic field (IMF). The motivation behind this is to move away from the index-driven paradigm and connect the diffusion process dynamics directly with primary characteristics of the SW. To the best of our knowledge this has not been demonstrated before and it is a novel approach offering improved performance and capabilities. Regarding the operational aspect we aimed in developing a model which can be used with widely available historical SW parameters (hindcast), with real-time SW measurements (nowcast), as well as in conjunction with models which can forecast these SW variables with prediction horizons of up to a few days, see for example, Samara et al. (2021) and discussion therein. The core of the model consists of an ensemble of probabilistic NNs trained with the D_{LL} dataset which was created in the framework of the Horizon 2020 SafeSpace project. Using the SW parameters the model provides expected (mean) values for both the electric and magnetic component of the D_{LL} as well as uncertainties on the provided mean values themselves, in the form of standard deviations. This allows the formulation of a probabilistic D_{LL} output and the definition of confidence levels which is particularly useful for forecasting systems which aim to provide users with more elaborate information to base decisions upon.

2. Data

In this study we make use of the extended SafeSpace radial diffusion coefficients database (Katsavrias et al., 2022), which is publicly available at https://synergasia.uoa.gr/modules/document/?course=PHYS120 and contains ~79,000 hourly D_{LL} values that span 9 years (2011–2019). These D_{LL} have been calculated directly from in-situ magnetic and electric field measurements, exploiting the fluxgate magnetometers (Auster et al., 2008) as well as the EFI instruments (Bonnell et al., 2008) on board the three THEMIS spacecraft (THEMIS A, D, and E). In this dataset the magnetic and the electric component of the D_{LL} (henceforward D_{LL}^B and D_{LL}^E, respectively), have

been calculated separately, based on the theoretical approach by Fei et al. (2006). We note that even though Fei's approach can lead to an underestimation of the total diffusion coefficient by a factor of two, due to the assumption of electric and magnetic field independence (Lejosne, 2019), it is still more widely used due to the fact that it is very difficult to separate the total measured electric field from single point measurements in space into its convective and inductive components (Lejosne & Kollmann, 2020). Furthermore, it has been shown that this discrepancy by a factor of 2 is minor relative to the large variability in the observed values (Sandhu et al., 2021).

Here we use hourly measurements each of which contains data for L* values in the [3-7] range divided into 40 bins with dL* = 0.1. As centroids we use the mean of the bin values, 3.05, 3.15 etc. The total D_{LL} can be simply calculated as the sum of the two components as shown in Equation 2.

$$D_{LL} = D^{B}_{LL} + D^{E}_{LL} \tag{2}$$

Moreover, D^{B}_{LL} has been calculated for 36 values of the first adiabatic invariant (μ) in the [300–20,000] MeV/Gauss range, corresponding to relativistic electrons with $E > 400$ keV at the aforementioned L* range (see also Figure S1).

This dataset is complemented with 1-hr resolution historical measurements of the SW speed (Vsw) and density (Nsw), the magnitude of the IMF and the Kp index (for the estimation of the D_{LL} from semi-empirical [SE] models) as provided by the OMNIWeb service of the Space Physics Data Facility at the Goddard Space Flight Center (http://omniweb.gsfc.nasa.gov/). For the calculation of the magnetic coordinates we have used the International Radiation Belt Environment Modeling (IRBEM) library (Bourdarie & O'Brien, 2009) and the Olson Pfitzer quiet external magnetospheric field model (OP77). The D_{LL} and SW parameters from the SafeSpace database are used for the training of the NNs with the latter being used to define inputs and the former the outputs.

We pre-process the D_{LL} values by applying a moving mean window containing the current hour and the previous 23 hr. This is done in order to mitigate the uncertainties introduced by the partial azimuthal coverage in the D_{LL} data derivation (see also Section 3 in Katsavrias et al., 2022) as well as fill the gaps in L* which are inherently present due to the THEMIS spacecraft orbit. The application of this moving mean can be roughly considered a trade-off, where some temporal resolution is sacrificed in order to increase the azimuthal one. We note that the temporal variance of the D_{LL} is evidently logarithmic and therefore the moving mean is applied on the log values of the D_{LL}. It is noted that for training and testing we use only values that were initially not empty except otherwise stated. For the same time window of the current and previous 23 hr we calculate the mean, the 25th and 95th quantiles, and the standard deviation (stdev) from the logarithms of each of the three SW variables (i.e., Vsw, Nsw, and IMF), thus having a total of 12 input parameters. These are the main inputs which are used for the estimation of the D_{LL}.

Furthermore, the L* parameter is also included as an input for the NNs and specifically its logarithm and the square of its logarithm. It is well known that D_{LL} has a very strong dependence on the L* parameter and several, if not all, widely used models to date use a parameterization of L* in analytical SE formulas, typically in the form of a power-law, for example, Ozeke, Boscher, Brautigam and Albert. Our objective is to construct a model which can provide D_{LL} estimations for any L* value, in contrast to a predefined rigid grid, and therefore it is included as an input parameter itself. This approach is often named "degridification" and it has been used in other modeling efforts, see for example, Bortnik et al. (2016); Katsavrias et al. (2021).

Finally the model is trained to estimate the electric component D^{E}_{LL} and the magnetic component D^{B}_{LL} at $\mu = 1{,}000$ MeV/G using the SW inputs. It is noted that the model D^{B}_{LL} outputs are then extended for the whole μ range, this is discussed further below.

3. Methodology and Machine Learning Model

3.1. Model Structure and Outputs

The architecture of a single network is shown in Figure 1 and it can be seen it is a feedforward net with multiple hidden layers. The activation function used is the LeakyReLu function which has been shown to perform well in regression tasks, typically outperforming the more traditional sigmoid functions and the original ReLu. Additionally, batch normalization (Ioffe & Szegedy, 2015), is applied at each layer prior to the non-linearities. The number

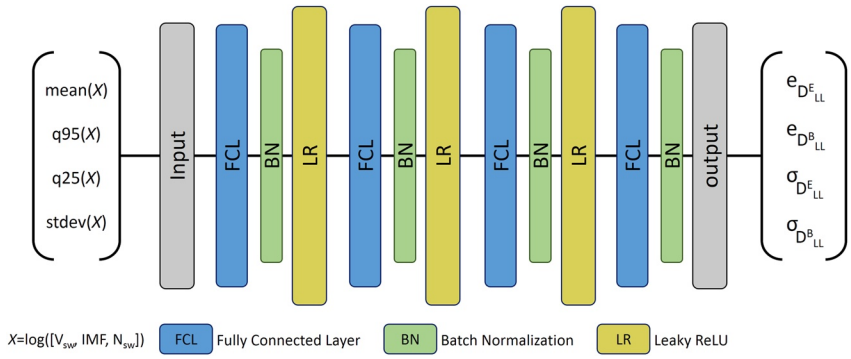

Figure 1. The architecture of a single neural network from the ensemble used in the model.

of neurons in the first layer is set to three times the input size (3 × 36) the middle layer consists of 200 neurons and the last layer to two times the input size (2 × 24) followed by the output layer which provides 4 outputs. The structure and the hyperparameters were optimized empirically with a sparse-grid approach. The network outputs are estimations of the logarithms of the electric and magnetic component of the D_{LL} (eE, eB), along with their respective logarithmic standard deviations (σE, σB). The cost function used is the Gaussian log-likelihood seen below in Equation 3.

$$Cost = \frac{1}{2}\sum_{i=1}^{N}\left[\log\left(\sigma_i^2\right) + \frac{(y_i - e_i)^2}{\left(\sigma_i^2\right)}\right] \tag{3}$$

Where N is the number of variables, in this case 2, (D_{LL}^E and D_{LL}^B), y_i are the logarithms of the training data, e_i the estimations of the network, and σ_i the standard deviations of the estimations. It can be seen that the cost function essentially consists of the simplified logarithm of a Gaussian. The function incorporates in the numerator of its second term the mean square error (MSE) which is the most commonly used cost function for regression tasks, but here it is modified by the presence of the stdev in the denominator. During training, the network is optimized to minimize the MSE and the stdev at the same time. It is noted that the latter cannot become arbitrarily large; while the second term would tend to zero resulting in a very low loss, the first term would tend to infinity countering the effect. This means that a trained network will always output a finite and non-zero stdev which is interpreted as the confidence the network has for its estimations of the D_{LL} values, or as a quantification of the epistemic uncertainty of the network output. Using the mean and stdev from the model outputs, a normal distribution can be directly calculated and quantiles for the estimations can be derived for each component at each timestep. For the calculation of the total D_{LL} random samples are derived for the two components and all possible combinations are calculated from which quantiles are derived. The output of the model is thus probabilistic/stochastic rather than deterministic, in contrast to more typical regression models which do not offer any additional information other than the estimated values. For the model initialization and training, we have used the ADAM algorithm (Kingma & Ba, 2015) using early stopping with 10% of the training set used for the internal validation subset. Finally, the model is comprised of an ensemble of five such networks that produce outputs in parallel and the final output is the average of the individual ones. The use of an ensemble improves the robustness of the model and reduces the significance of the initial random state of a network's internal parameters (weights and biases).

3.2. Extension of D_{LL}^B Outputs in the μ Range

As discussed the NNs are trained to output D_{LL}^B values for μ = 1,000 MeV/G which is the geometric mean of the [300–20,000] MeV/G range of the dataset. In order to extend the D_{LL}^B output of the NNs to the whole μ range of [300–20,000] MeV/G a simple but effective regression scheme is used here. For each L*, normalized D_{LL}^B spectra are calculated by dividing the D_{LL}^B dataset spectra with their respective values at μ = 1,000 MeV/G.

As seen in Figure 2 the normalized spectra are very consistent for a given L* showing minimal divergences at the two ends of the μ range, effectively being all constrained within very narrow limits. We note this is fully expected as the D_{LL}^B in the dataset is calculated as a function of μ, for details see the discussion in Katsavrias et al. (2022).

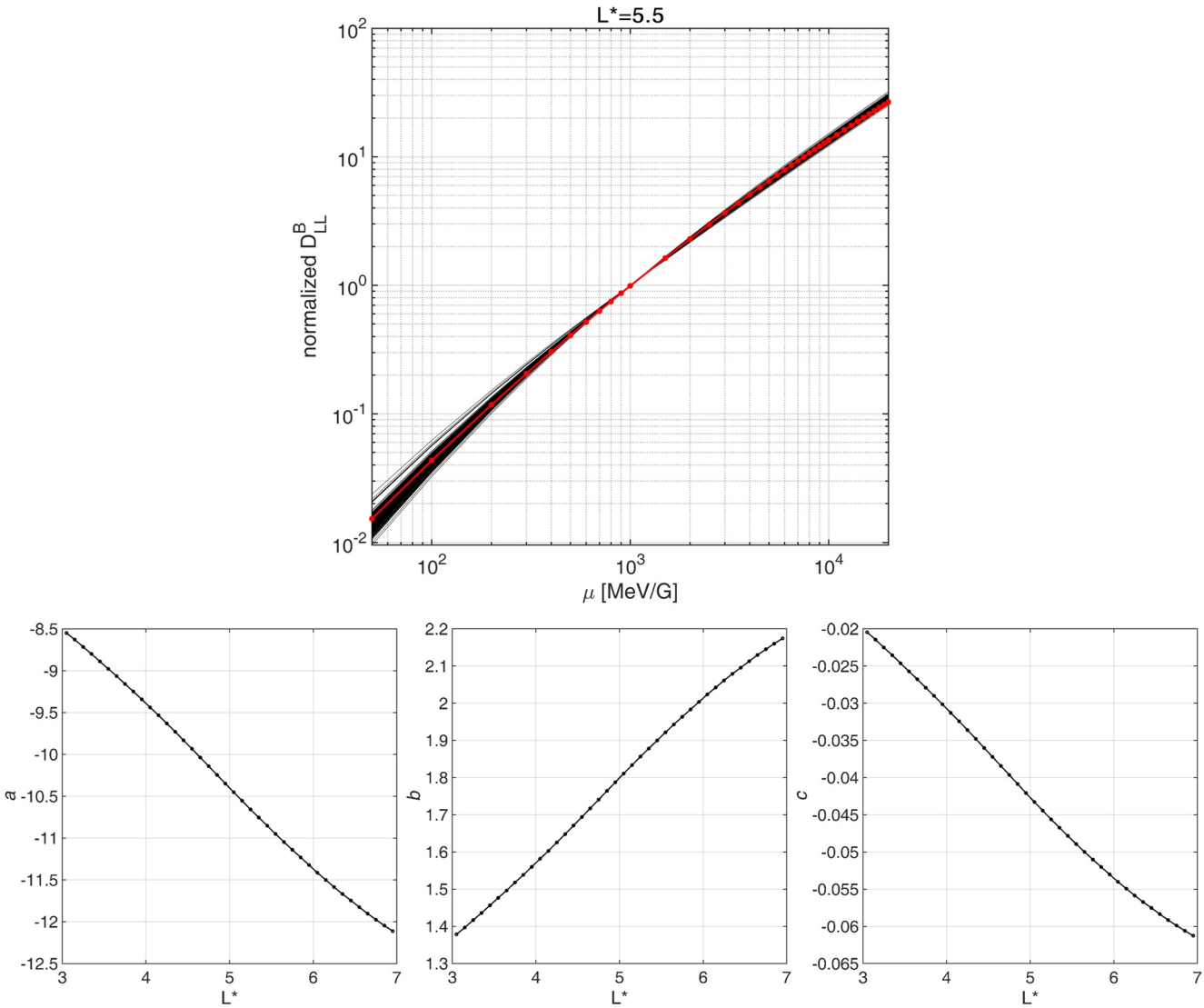

Figure 2. (Top panel): All normalized D^B_{LL} spectra from the dataset and the analytical fit for L* = 5.5. (Bottom panels): the a–c, factors used for the calculation of the D^B_{LL} spectrum for the whole μ range as derived at all L* values.

The mean of all normalized spectra, for a given L*, is then fitted with an analytical function of μ which can adequately describe it; we have used here a quadratic function in log-space seen below in Equation 4.

$$\log\left[normD^B_{LL}(\mu, L^*)\right] = a(L^*) + b(L^*)\cdot\log(\mu) + c(L^*)\cdot\left[\log(\mu)\right]^2 \quad (4)$$

The a–c fit parameters are calculated for each L* and they demonstrate smooth profiles as seen in Figure 2 allowing a safe interpolation for any L*. With this scheme, the values estimated from the model at 1,000 MeV/G can be used to directly calculate the D^B_{LL} spectrum for the whole μ range by using the fit parameters and performing this process in reverse.

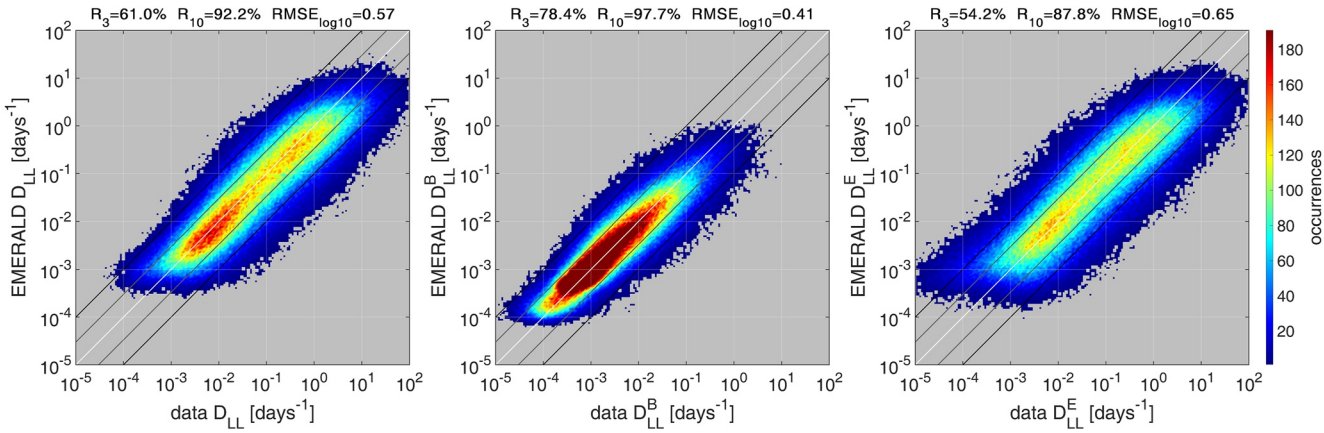

Figure 3. Density cross-plots for the electric (left panel) and magnetic (middle panel) components, as well as the total D_{LL} (right panel) at 1,000 MeV/G showing comparisons of the median estimations from the model with the data. The white, gray and black solid lines correspond to the equality line, factor of 3 and factor of 10, respectively.

4. Results

4.1. Model Performance

4.1.1. D_{LL}^{E}, D_{LL}^{B} and Total D_{LL} Estimation

We evaluate the performance of the model on the estimation of D_{LL}^{E} and D_{LL}^{B}, as well as the total D_{LL}, by using a leave-one-out cross-validation scheme. This is a typical approach for evaluating a trained model on the entirety of a dataset without the need for additional reference data, see for example, Aminalragia-Giamini et al. (2021) and is detailed in the steps below. We divide here the data in nine calendar years (2011, 2012, …, 2019), and for each year we train the model with the other 8 years and then test it with the one left out. We iterate this process over the 9 years of the dataset and train a different NN ensemble in each iteration which then provides D_{LL} outputs for the left-out year.

1. The algorithm defines a specific calendar year and isolates the corresponding hourly D_{LL} as well as the input parameters.
2. The training of the NNs is performed with the rest of the dataset. For example, if we consider the year 2011, the training will be made using the D_{LL} values and SW parameters from the 2012–2019 time period.
3. The now trained model from the previous step is used to estimate the D_{LL} values of the excluded year using the also excluded input parameters.
4. The process repeats iteratively for all the available years in the dataset.

This way, in each iteration we test our model with data it has not been trained with and after all iterations we have derived outputs for the entirety of the dataset. Crucially, this approach ensures an objective and fair evaluation of the model performance.

Figure 3 shows density plots for the electric and magnetic component at 1,000 MeV/G, as well as the total D_{LL}, with comparisons of the data and the medians derived from the models outputs at all L* bins. For the density plots we have used 200 logarithmic bins, equality lines are in white, dark gray lines denote a factor of 3, and black lines a factor of 10. The density plots also show metrics from the comparisons, where R_3 is the percentage of model values being within a factor of 3 of the dataset values, R_{10} is the same for a factor of 10, and $RMSE_{log10}$ is the root mean square error (RMSE) calculated for the log-base-10 values. The results show that the D_{LL} and its components are estimated from the SW with a high degree of accuracy. In all three cases more than 50% of the values are within a factor of 3 while more than ∼88%, and up to ∼98%, of the values are within a factor of 10 the data. The highest densities appear along the equality lines with clear linear/log-linear trends seen across several orders of magnitude. It is noteworthy that the two D_{LL} components are not equally well estimated, with D_{LL}^{B} at 1,000 MeV/G showing less scattering, higher clustering along the equality line, and better metrics overall. This is expected and understood by the fact that D_{LL}^{B} was shown in Katsavrias et al. (2022) to have stronger correlations with the used SW variables. It is also worth mentioning that there are deviations at the lowest values

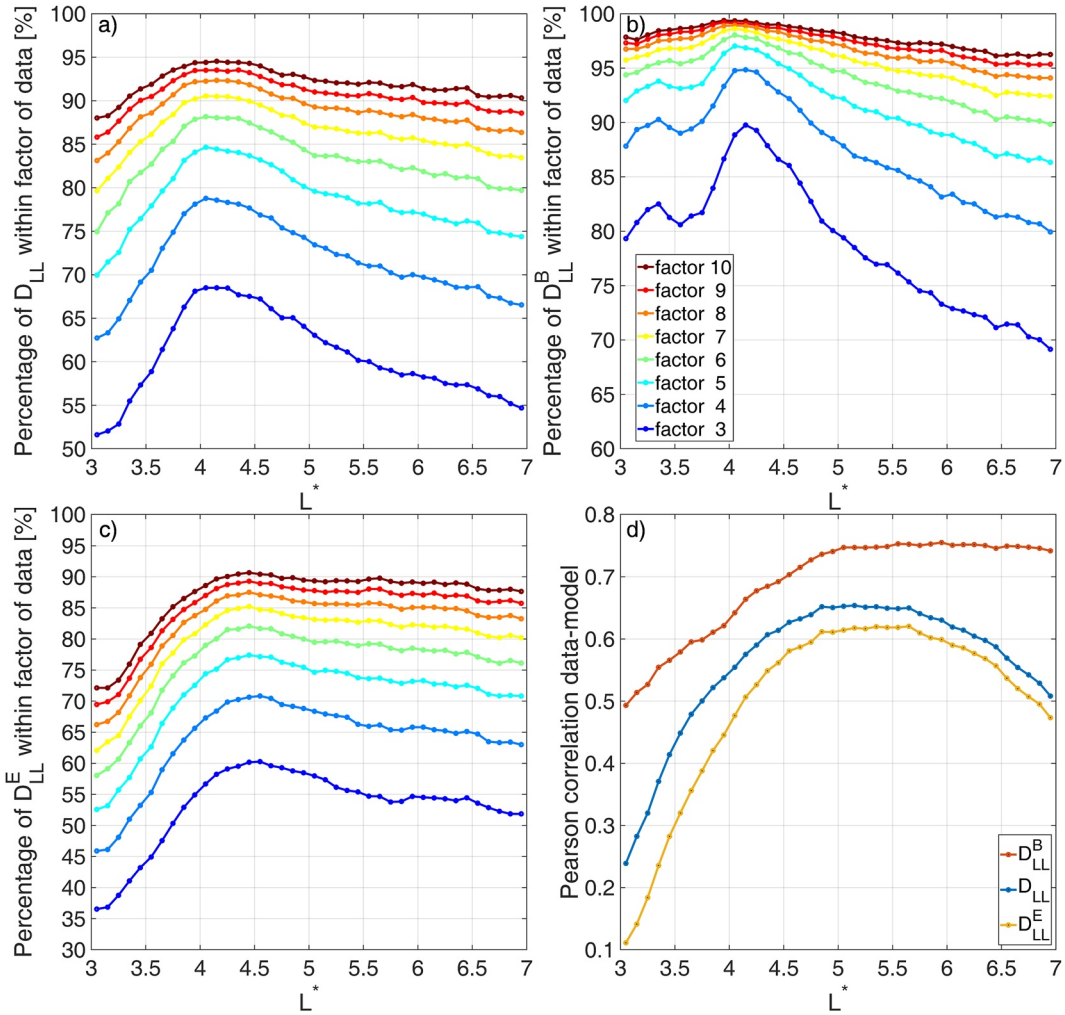

Figure 4. (a–c) Curves of percentages of median model outputs that are within a factor of the data as a function of L*. (d) Pearson correlation of logarithmic values of data and median model outputs as a function of L*.

where background tails can be seen, especially for D^E_{LL}, and some underestimation on some of the highest values. However, even in these cases these areas are of very low density and the majority of the values are within the denoted limits.

We also investigate in more detail the performance of the model with respect to L*. Figure 4 shows the percentage of the model's median outputs that are within a factor of $x = 3, 4, 5,\ldots,10$ of the data as a function of L* for the whole [3, 7] range and the Pearson correlation coefficients calculated for the logarithmic values of the data and the model outputs. For both D^E_{LL} and D^B_{LL} at 1,000 MeV/G, and total D_{LL}, it can be seen that the model performs optimally for L* values roughly in the [4, 6] range, that is, for the core of the outer belt. This is primarily attributed to the correlation of the D_{LL} components with the SW parameters we use as inputs, where the highest correlations for both D_{LL} components occur roughly in the same [4, 6] L* range (Katsavrias et al., 2022). Therefore the peak performance of the model is indeed expected to be found in this range.

An additional important reason is that the amount of available data at L* values lower than ∼4 is reduced in the dataset (see also Figure S2) resulting in the model having less data in this region to be trained with. Data at lower L* values were originally removed from the dataset due to the effects of magnetic field gradients which make an accurate derivation of D_{LL} coefficients very difficult (see also Section 2.1 in Katsavrias et al. (2022)). Finally, for higher L* values (L* > 6), an additional potential reason for the comparatively lower performance are the uncertainties in the L* derivation introduced by the use of the Olson-Pfitzer quiet model. These uncertainties, which are not trivial to quantify and beyond the scope of this work, are expected to affect more D^B_{LL} compared

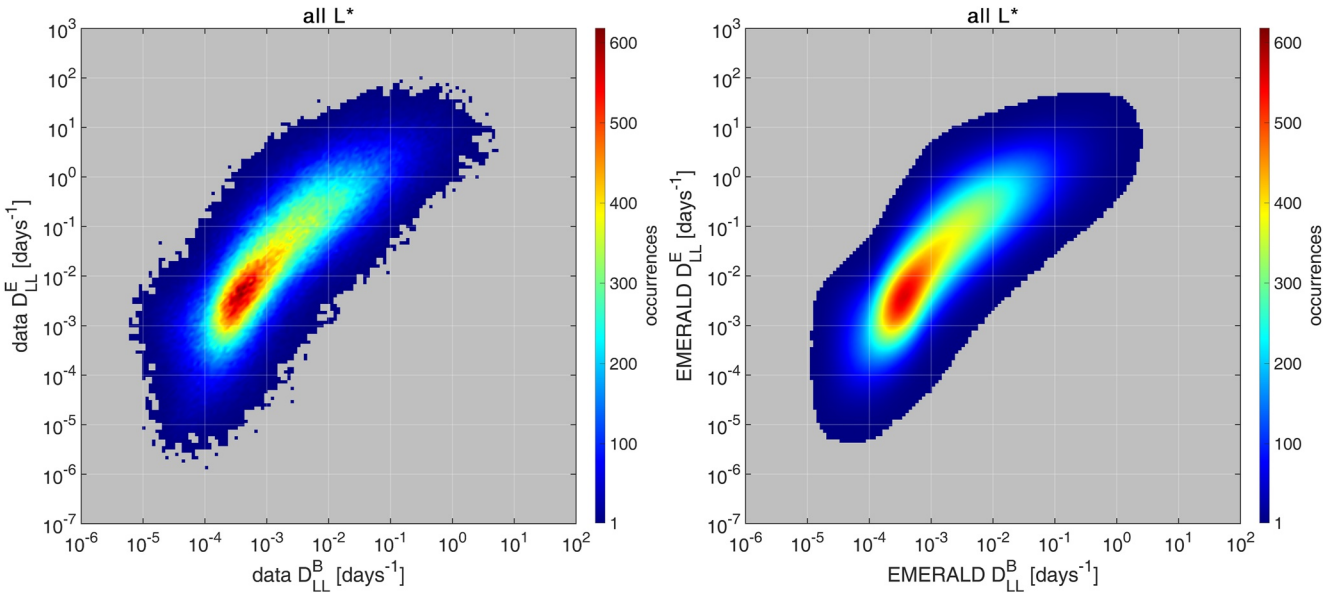

Figure 5. D_{LL}^B versus D_{LL}^E density plots in logarithmic scale. Left are the dataset values and right the values derived from the model outputs.

to D_{LL}^E, as is indeed seen, since the former is primarily driven by ULF waves generated at high L-shells by SW pressure pulses. However, we note that the lower performance is primarily seen for factors 3, 4, and 5, while the differences are much smaller across L* for higher factors.

Overall, there is a large jump in performance going from a factor of 3 to factor of 4 while more than 90% of the model outputs are within a factor of 10 of the data in almost all cases. Furthermore the Pearson correlation shows again that D_{LL}^B is estimated optimally, and for the total D_{LL} the model achieves significant correlations r > 0.5 for L* values above ∼3.75. These results illustrate that the model can successfully estimate D_{LL} solely from SW parameters while achieving good accuracy. Finally we must note that the performance for D_{LL}^B at all μ values is very similar with the one shown here at 1,000 MeV/G. This is important, as for higher μ values D_{LL}^B becomes on average comparable and then dominant with respect to D_{LL}^E, and the total D_{LL} behavior resembles that of the former increasingly. While the opposite is also true for lower μ values, this means that for the largest part of the μ range of [300–20,000] MeV/G we use here, the total D_{LL} performance is even better than that of 1,000 MeV/G, as shown further below.

4.1.2. Reproduction of the Relationship of D_{LL}^E and D_{LL}^B

The model's simultaneous estimation of both D_{LL}^E, and D_{LL}^B allows us to investigate here whether the model outputs reproduces any relationship of D_{LL}^E and D_{LL}^B as existing in the dataset. It is noteworthy that the relationship of the two components is not broadly investigated in the literature with only a few recent works reporting on quantitative comparisons, such as Sandhu et al. (2021) and Katsavrias et al. (2022). Moreover most established models directly estimate the total D_{LL} making investigation of this relationship impossible in these cases. The modeling approaches of Ali et al. (2016) and Ozeke et al. (2014) do estimate separately both D_{LL}^B and D_{LL}^E but, including these works, we cannot find in the literature any such investigations. Therefore, to the best of our knowledge this is the first time the D_{LL}^B-D_{LL}^E relationship is demonstrated to be successfully modeled.

Figure 5 shows density plots of D_{LL}^B at 1,000 MeV/G versus D_{LL}^E for the data values and the values predicted from the model in 150 logarithmic bins. For each prediction of the model 200 randomly sampled values are derived using the predicted means and stdevs of D_{LL}^B and D_{LL}^E, and of those we keep the 180 that are within the 5th and 95th quantiles to avoid errantly large or small samples. The occurrences for the model are normalized with this factor. It is seen that the model outputs reproduce very well the inter-relationship of the two D_{LL} components across several orders of magnitude of values. The trend between the two variables is clearly visible and well represented in the model outputs. Even features at very low densities of occurrence such as the "shoulder" at low D_{LL}^B values (∼10^{-4} days^{-1}) and moderate D_{LL}^E values (∼10^{-1} days^{-1}) and the light blue "halo" around the denser (cyan to red) areas are clearly seen in the model outputs. Finally, in the denser areas with the highest occurrences

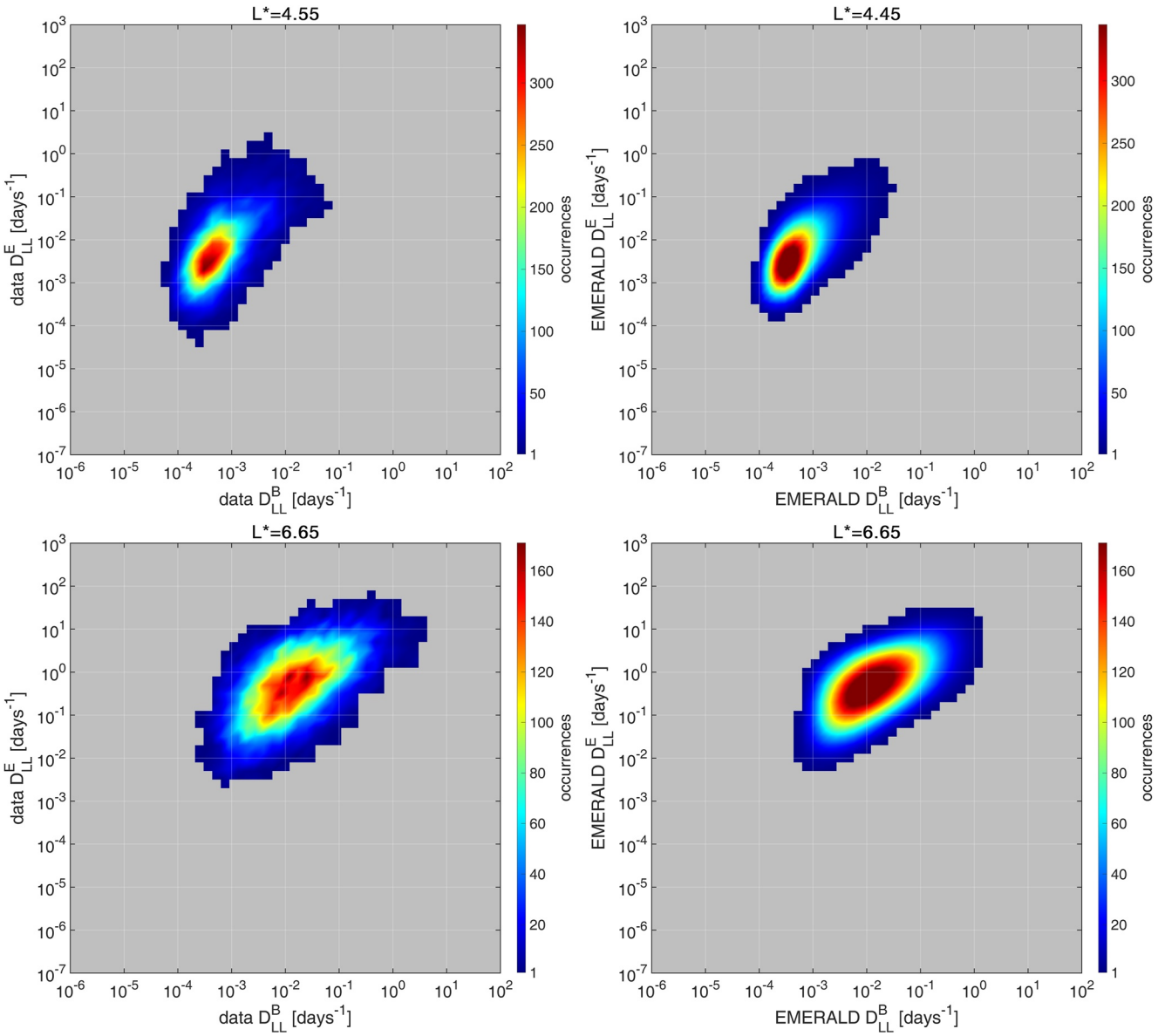

Figure 6. D_{LL}^{B} versus D_{LL}^{E} density plots in logarithmic scale at L* = 4.55 and L* = 6.65 for the data and the model outputs.

there is remarkable agreement with the model outputs essentially producing a smoothed version of the data distribution.

Moreover, the relationship of the two components varies with L* and we show that the model captures this behavior beyond the overall comparison for all L* values. Figure 6 shows two examples for L* = 4.55 and L* = 6.65. It is seen that for the different L* values the distributions are very different; both in terms of absolute values as expected, and more importantly here, in terms of the relationship of the two components. However in both cases the model-derived values reproduce well the distributions of the data.

4.2. Comparisons of Total D_{LL} With Semi-Empirical Models

In this section we perform comparisons of the total D_{LL} from the dataset with the outputs of the Electric and MagnEtic RAdiaL Diffusion (EMERALD) model and two established SE models, namely the Brautigam & Albert (B&A) model (Brautigam & Albert, 2000), and the Ozeke model (Ozeke et al., 2014). The parameterizations of

the models are seen in Equations 5–7 below. We have applied the previously discussed 24 hr moving mean on the SE D_{LL} values so as the comparisons will be fair to the SE models.

$$D_{LL}^{EM}[BA] = 10^{(0.506 \cdot Kp - 9.325)} \cdot L^{10} \quad (5)$$

$$D_{LL}^{B}[OZ] = 6.62 \cdot 10^{-13} \cdot 10^{(-0.0327 \cdot L^2 + 0.625 \cdot L - 0.0108 \cdot Kp^2 + 0.499 \cdot Kp)} \cdot L^{8} \quad (6)$$

$$D_{LL}^{E}[OZ] = 2.16 \cdot 10^{-8} \cdot 10^{(0.217 \cdot L + 0.461 \cdot Kp)} \cdot L^{6} \quad (7)$$

We present results for several values of μ in order to cover a wide range. We note that as the NN ensemble outputs the D_{LL}^{B} at 1,000 MeV/G these results at different μ values include the D_{LL}^{B} regression scheme discussed previously. The comparisons are made for the whole dataset as well as for a time period of three consecutive geomagnetic storms which occurred during December 2013 and resulted in some of the highest D_{LL} values of our dataset. Additionally we have examined a quiet period from December of 2012 to January of 2013. The quiet period was selected due to the absence of significant geomagnetic activity as well as both chorus and ULF wave activity (Jaynes et al., 2014). These two time periods are examined complementarily to the whole dataset comparisons in order to illustrate in more detail the model performance in shorter time scales.

4.2.1. Comparisons for All Values of the Dataset

Figure 7 shows density cross-plots with comparisons at three μ values, 500, 3,000, and 10,000 MeV/G, of total D_{LL} with the model's median output and D_{LL} values calculated from the SE models. We note that as the latter ones do not include a μ dependence only the data they are compared with change. There are several observations to be made here. The first one is that similar to what was shown at Figure 3 for 1,000 MeV/G our model shows a consistent linear/log-linear relationship with the data for all μ values and across several orders of magnitude capturing the full L* range. Its performance, as quantified by the R_3, R_{10}, and RMSE metrics, is only slightly lower for 500 MeV/G than for 1,000 MeV/G whereas it improves for higher μ values as the magnetic component becomes more dominant in the total D_{LL}. We note there is a systematic overestimation at the lower extreme of the distribution at very low D_{LL} values with the formation of a "background tail", for example, below 10^{-3} days^{-1} at 3,000 MeV/G. This is primarily related to low L* values, which also have lower D_{LL} values, and occurs for reasons previously discussed in Section 4.1.1.

Apart from this, the overall model's performance remains consistently good for all cases. The high density areas are always clustered along the equality lines and the majority of values is within a factor of 3 of the data with the remaining cases being again predominantly within a factor of 10 while also achieving good RMSE scores. However, this is not the case with the D_{LL} values from the SE models. As there is no μ dependence these models cannot capture this dependence of the D_{LL} and show increasingly large deviations as μ also increases quantified in the shown metrics. Furthermore there are clear trends which deviate from the ideal linear/log-linear relationship with the data; apart from the absolute magnitude of D_{LL}, the SE models systematically underestimate the low and high values relative to values close to the mean. This results in a non-linear relationship with the data and a characteristic curve seen here. These findings on the SE models are in agreement with Katsavrias et al. (2022) and can be explained by the fact that these Kp-driven formulations have been derived from analytical fits to long-term averages. Due to this, the divergence of the lower and upper ends of the D_{LL} distribution cannot be well taken into account and such fits will be dominated by the large majority of values that are closer to the mean or median. However, our model does not use such long-term averages and is able to capture optimally the behavior of the D_{LL} using the SW parameters as input.

4.2.2. Comparisons for a Radiation Storm Event and a Quiet Period

Figure 8 shows the comparison of the EMERALD D_{LL} with the data D_{LL} values and the SE models of Brautigam & Albert and Ozeke during the December 2013 period. The comparison is performed for μ = 500 MeV/G at L* = 6.45 (~500 keV) and for μ = 5,000 MeV/G at L* = 4.45 (~3 MeV), corresponding respectively to low energy particles' inward transport from the outer boundary, and diffusion of relativistic and ultra-relativistic electrons in the heart of the outer belt. As shown, the median output of EMERALD can capture both the dynamic evolution of the D_{LL} as well as its magnitude in both pairs of μ and L* values, compared with the SE models (Table 1).

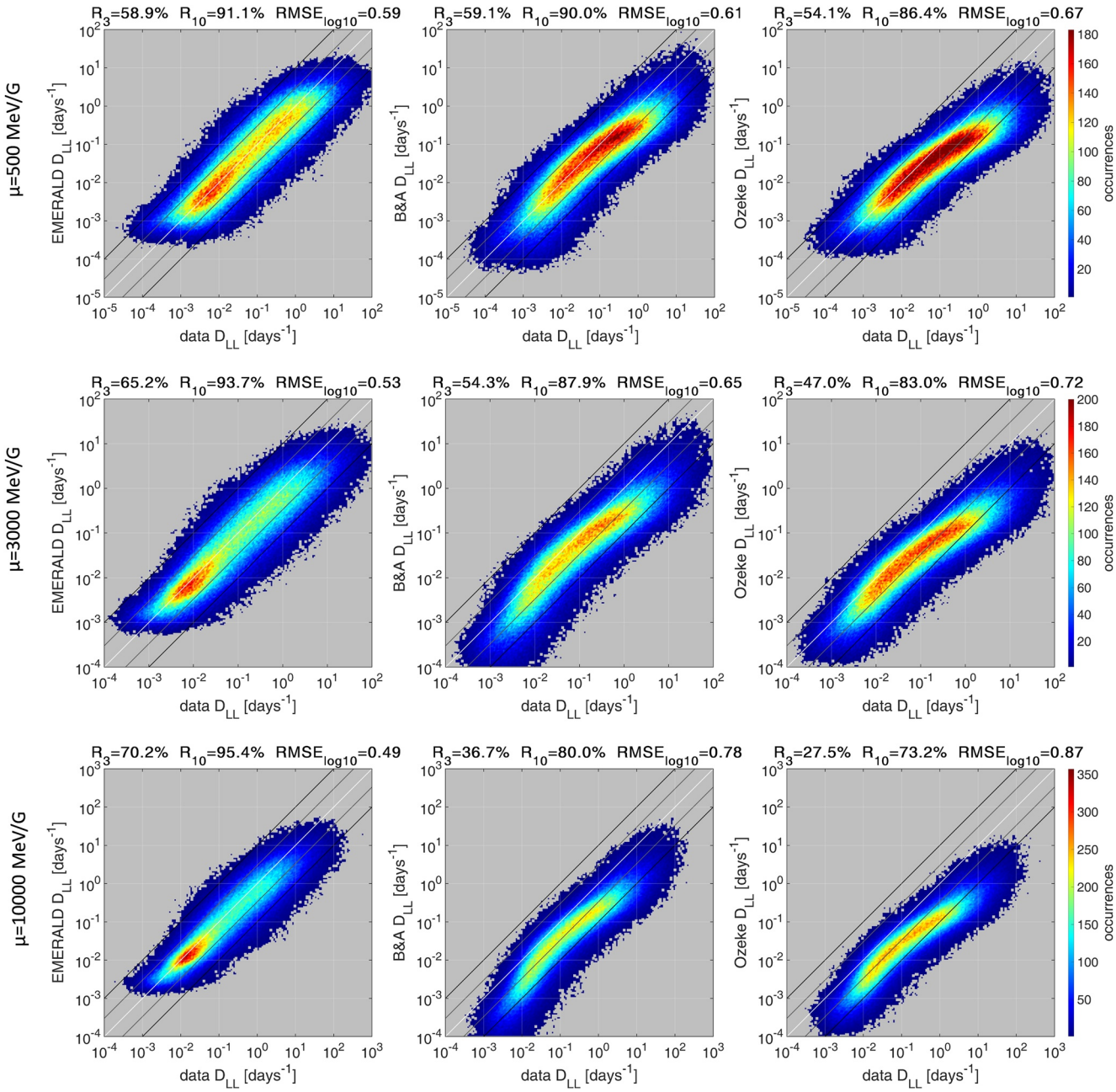

Figure 7. Density cross-plots for total D_{LL} showing comparisons of the data with the model's median output and the Brautigam and Albert and Ozeke models at μ values of 500 MeV/G (top row panels), 3,000 MeV/G (middle row panels), and 10,000 MeV/G (bottom row panels). The white, gray and black solid lines correspond to the equality line, factor of 3 and factor of 10, respectively.

In detail, concerning the 500 MeV/G at L* = 6.45, EMERALD reproduces quite well both the high and low D_{LL} values, while the majority (62.15%) of the estimations are within a factor of 3 of the data with the remaining cases being again predominantly within a factor of 10 (panel f). On the other hand, the two SE models exhibit very similar behavior between them, differing only by a small multiplying factor. Their behavior consistently underestimates the high D_{LL} values on average by a factor of 10 or more (panel g). Furthermore, the SE models fail to capture the low D_{LL} values, exhibiting a strong flattening behavior, which also contributes to the lower R_3 and higher RMSE values shown in Table 1. This comparison is in agreement with the results of Katsavrias et al. (2022) who illustrated, in the simulations of the March 2015 time period that the SafeSpace D_{LL} produced a more realistic radial transport of 500 keV electrons than the one produced by the SE model of Boscher

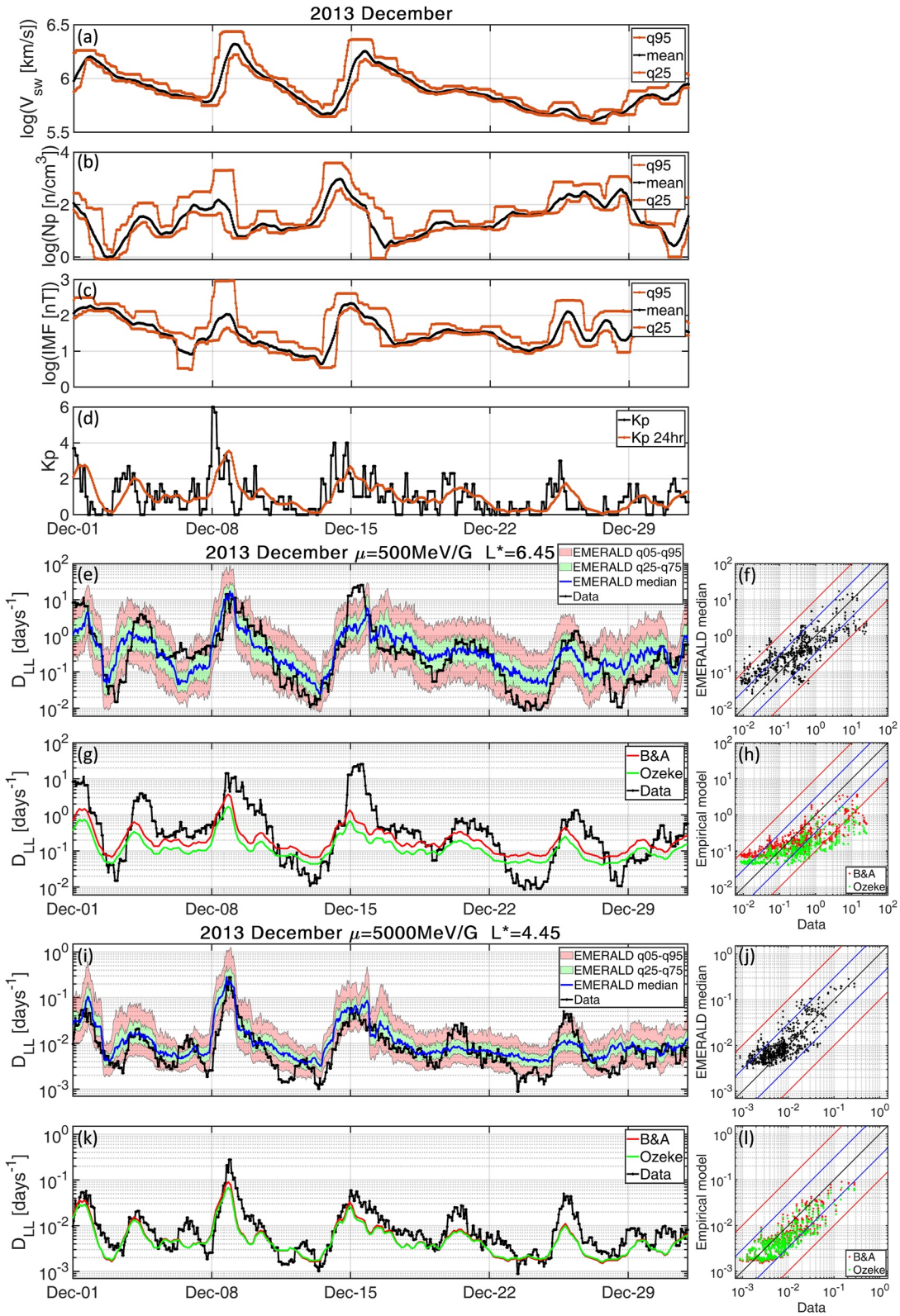

Figure 8. Timeseries and cross-plots of total D_{LL} for the December 2013 active period showing comparisons of the data with the model's median and quantile outputs and the 24 hr moving mean of the Brautigam Albert and Ozeke models at L* = 6.45 − μ = 500 MeV/G, and at L* = 5.45 − μ = 5,000 MeV/G. The black, blue, and red lines in the cross-plots correspond to the equality line, factors of 3 and 10, respectively.

Table 1
$RMSE_{log10}$ and Percentage of Points Within a Factor of 3 and 10 for the Electric and MagnEtic RAdiaL Diffusion (EMERALD), Brautigam & Albert and Ozeke Models During the December 2013 Time Period

	Model	R_3	R_{10}	$RMSE_{log10}$
L* = 6.45	EMERALD (median)	62.15	95.03	0.510
	B&A	59.32	92.35	0.571
μ = 500 MeV/G	Ozeke	46.17	86.84	0.678
L* = 4.45	EMERALD (median)	87.24	100	0.300
	B&A	88.99	100	0.300
μ = 5,000 MeV/G	Ozeke	86.57	100	0.310

et al. (2018), which shares strong similarities with the Brautigam & Albert formalization and model.

Concerning the 5,000 MeV/G at L* = 4.45, EMERALD successfully reproduces both the magnitude and dynamic evolution of the D_{LL} (panel i), while the large majority of the estimations (87.24%) are clustering along the equality line and within a factor of 3 (panel j). Once again, the two SE models exhibit very similar behavior and, even though they capture the dynamical behavior of the D_{LL} (panel k) and exhibit similar scores with EMERALD (Table 1), they consistently underestimate the D_{LL} values by approximately a factor of 2 (panel l). The underestimation of the higher and lower D_{LL} values by the SE models is in agreement with the results shown in Figure 7 for the 3,000 and 10,000 MeV/G. We note that the SE models results presented in Figure 8 correspond to a 24 hr moving mean, therefore the actual variation of the SE D_{LL} is much higher and follows the variation of the hourly Kp index shown in Figure 8d.

It is worth mentioning that even though the higher D_{LL} values as well as the general trend of EMERALD D_{LL} is primarily driven by Vsw (panel a), Nsw and IMF play a crucial role in capturing the small scale dynamics. Characteristic examples are the D_{LL} decrease which occurs on December 2 driven solely by Nsw and the D_{LL} increase on December 25-28 which is driven by both Nsw and IMF.

Similar to Figure 8, Figure 9 shows the comparison of the EMERALD D_{LL} with the data D_{LL} values and the 24 hr moving mean of the SE models of Brautigam & Albert and Ozeke during the 23 December 2012–12 January 2013 quiet period. Once again, concerning the 500 MeV/G at L* = 6.45, EMERALD reproduces quite well the dynamics of the D_{LL} values, closely following the decreases and increases while also showing a mostly linear/log-linear cross-plot (panel f). On the other hand, the two SE models fail to capture both the D_{LL} dynamics and magnitude (panel g) estimating values in a relatively narrow range and exhibiting a pronounced flattening (panel h). This difference is also illustrated in the scores shown in Table 2, where the SE models exhibit significantly higher RMSE values, compared to EMERALD, as well as lower R_3 and R_{10} values.

Concerning the 5,000 MeV/G at L* = 4.45, here all three models fail to capture the magnitude and the dynamic evolution of the D_{LL} values. The only exception is that EMERALD somewhat manages to reproduce the D_{LL} evolution on the final week of the data (6–13 January). The SE models again produce D_{LL} in a narrow range, following the very small variation of the Kp index (panel d), showing a mostly flat cross-plot (panel l), while they completely fail to capture the dynamics of the D_{LL} values, especially at the second half (after 1 January) of the examined time period. Their notably better scores ($R_3 \sim 88\%$ and RMSE ~ 0.32 as shown in Table 2) stem mostly from the fact that their values are closer to the overall mean of the data during this period for this combination of μ and L*.

The overestimation of the 5,000 MeV/G D_{LL} values in this very quiet period, especially for the first 2 weeks, is in agreement with the results of Figure 7 and a fair representation of our model's performance is part of the reason we have made these comparisons. The 5,000 MeV/G D_{LL} values in this period hover around 10^{-3} $days^{-1}$ which is at the lowest end of the distribution where the model tends to overestimate. We note however, that even here all the values are at most within a factor of 10.

The above discussed results, combined with the results shown in Figure 7 for the whole dataset, show that EMERALD outperforms the SE models in a wide μ and L* range, and emphasize the importance of modeling the D_{LL} μ dependence.

5. Conclusions

In this work, we have used the SafeSpace database of radial diffusion coefficients, spanning 9 years (2011–2019), and we have developed EMERALD, a NN based model for the estimation of the D_{LL} in the outer radiation belt, using solely SW parameters (Vsw, Nsw, IMF) and L* as an input. The approach we have employed is a significant departure from the common Kp-driven paradigm for the estimation of D_{LL}. Rather than using as driver of the model an index which is a proxy of the effects of SW on the global magnetospheric activity, we have directly

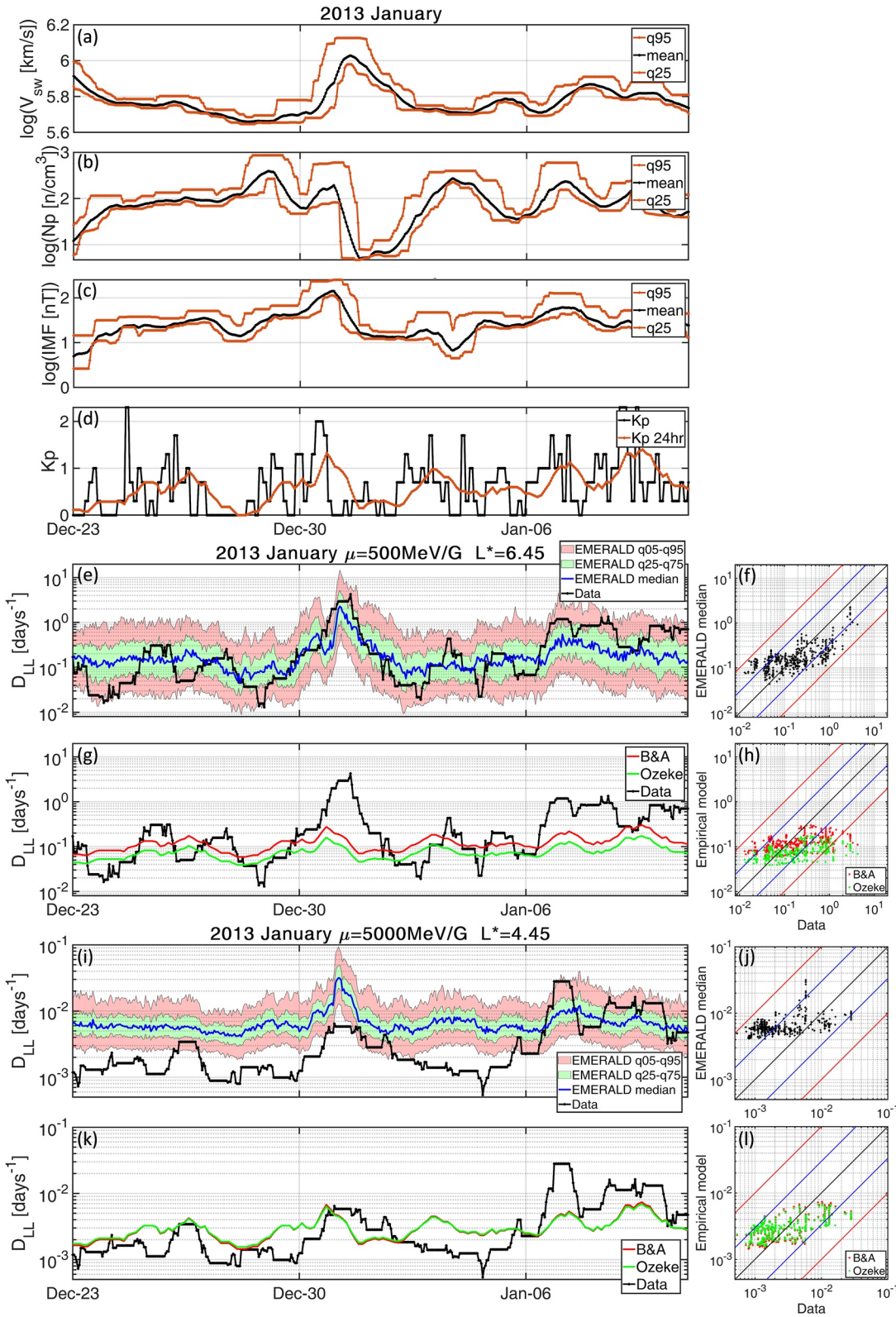

Figure 9. Same as Figure 8 for the 23 December 2012–12 January 2013, quiet period.

Table 2
Same as Table 1 for the 23 December 2012–12 January 2013 Quiet Period

	Model	R_3	R_{10}	$RMSE_{log10}$
L* = 6.45	EMERALD (median)	71.33	100	0.412
	B&A	65.42	95.40	0.508
μ = 500 MeV/G	Ozeke	59.51	87.30	0.607
L* = 4.45	EMERALD (median)	46.38	99.78	0.530
	B&A	88.18	100	0.32
μ = 5,000 MeV/G	Ozeke	87.96	100	0.326

connected SW characteristics to the evolution of the radial diffusion process. The use of these specific SW parameters is based on the correlation analysis by Katsavrias et al. (2022). The latter authors discussed the correlation of the aforementioned parameters with the D_{LL} components and linked them with the two main physical mechanisms that enhance the ULF wave power, that is, the Kelvin-Helmholtz instabilities and the SW pressure pulses. This is in agreement with the results of Bentley et al. (2018) who indicated that ULF wave power increases for increasing Vsw, strongly negative Bz, and increasing perturbations in Nsw. Special reference should be made to the significance of SW speed which is shown to be crucial for recent modeling efforts of the outer radiation belt electrons (Chu et al., 2021; Katsavrias et al., 2021; Smirnov et al., 2020). We must emphasize that even though geomagnetic indices, such as SYM-H and AE, have been shown to also correlate well with the D_{LL} components, they are not used as inputs in this model. Beyond the discussed aim of this work another practical reason for this is the fact that these indices are not provided in near real-time and thus the model would lack the ability of estimating the D_{LL} in a nowcasting or forecasting framework.

EMERALD provides estimations of the radial diffusion coefficients in a broad L* range [3–7] covering the outer radiation belt including the geosynchronous orbit. The two D_{LL} components (electric and magnetic) are estimated separately but simultaneously, thus maintaining the coherency and interrelationship between them. The model, also provides energy (μ) dependence for the magnetic D_{LL} in the (300–20,000 MeV/G) range. This is especially important for high μ values where D_{LL}^{B} is on average comparable or higher than D_{LL}^{E} and for periods with intense magnetospheric compression, where the total D_{LL} can be dominated by the magnetic component even at low μ values (Katsavrias et al., 2022; Thanasoula et al., 2022).

Comparisons with established SE models show that EMERALD can successfully estimate the total D_{LL} achieving equal and mostly higher performance. Thus, it can be used to optimally estimate the process of radial diffusion in radiation belt dynamics in conjunction with physics-based models. Finally, the probabilistic approach adopted for the model provides confidence levels of the D_{LL} estimations. These are important in quantifying the uncertainties of the estimations, and moreover such outputs can be readily used in data assimilation tools, employed by many recent space weather prediction efforts.

Data Availability Statement

The D_{LL} dataset used for the training of EMERALD can be found in https://synergasia.uoa.gr/modules/document/index.php?course=PHYS120. The authors acknowledge the THEMIS/FGM and THEMIS/EFI teams for the use of the corresponding datasets which can be found online in http://themis.ssl.berkeley.edu/data_products/index.php, the developers of the International Radiation Belt Environment Modeling (IRBEM) library and the NASA/GSFC's Space Physics Data Facility's OMNIWeb service in https://spdf.gsfc.nasa.gov/pub/data/omni/high_res_omni/.

Acknowledgments
This work has received funding from the European Union's Horizon 2020 research and innovation programme "SafeSpace" under grant agreement no 870437. The authors would also like to thank the editor and two anonymous referees whose comments helped improve the manuscript.

References

Ali, A. F., Malaspina, D. M., Elkington, S. R., Jaynes, A. N., Chan, A. A., Wygant, J., & Kletzing, C. A. (2016). Electric and magnetic radial diffusion coefficients using the Van Allen probes data. *Journal of Geophysical Research: Space Physics*, *121*(10), 9586–9607. https://doi.org/10.1002/2016ja023002

Allison, H. J., & Shprits, Y. Y. (2020). Local heating of radiation belt electrons to ultra-relativistic energies. *Nature Communications*, *11*(1), 4533. https://doi.org/10.1038/s41467-020-18053-z

Aminalragia-Giamini, S., Raptis, S., Anastasiadis, A., Tsigkanos, A., Sandberg, I., Papaioannou, A., et al. (2021). Solar energetic particle event occurrence prediction using solar flare soft X-ray measurements and machine learning. https://doi.org/10.1051/swsc/2021043

Auster, H. U., Glassmeier, K. H., Magnes, W., Aydogar, O., Baumjohann, W., Constantinescu, D., et al. (2008). The THEMIS fluxgate magnetometer. *Space Science Reviews*, *141*(1–4), 235–264. https://doi.org/10.1007/s11214-008-9365-9

Bentley, S. N., Watt, C. E. J., Owens, M. J., & Rae, I. J. (2018). Ulf wave activity in the magnetosphere: Resolving solar wind interdependencies to identify driving mechanisms. *Journal of Geophysical Research: Space Physics*, *123*(4), 2745–2771. https://doi.org/10.1002/2017JA024740

Beutier, T., & Boscher, D. (1995). A three-dimensional analysis of the electron radiation belt by the salammbô code. *Journal of Geophysical Research*, *100*(A8), 14853. https://doi.org/10.1029/94JA03066

Bonnell, J. W., Mozer, F. S., Delory, G. T., Hull, A. J., Ergun, R. E., Cully, C. M., et al. (2008). The electric field instrument (EFI) for THEMIS. *Space Science Reviews*, *141*(1–4), 303–341. https://doi.org/10.1007/s11214-008-9469-2

Bortnik, J., Li, W., Thorne, R. M., & Angelopoulos, V. (2016). A unified approach to inner magnetospheric state prediction. *Journal of Geophysical Research: Space Physics*, *121*(3), 2423–2430. https://doi.org/10.1002/2015ja021733

Boscher, D., Bourdarie, S., Maget, V., Sicard-Piet, A., Rolland, G., & Standarovski, D. (2018). High-energy electrons in the inner zone. *IEEE Transactions on Nuclear Science*, *65*(8), 1546–1552. https://doi.org/10.1109/tns.2018.2824543

Bourdarie, S., & O'Brien, T. (2009). International radiation belt environment modelling library. *Space Research Today*, *174*, 27–28. https://doi.org/10.1016/j.srt.2009.03.006

Brautigam, D. H., & Albert, J. M. (2000). Radial diffusion analysis of outer radiation belt electrons during the October 9, 1990, magnetic storm. *Journal of Geophysical Research*, *105*(A1), 291–309. https://doi.org/10.1029/1999ja900344

Camporeale, E., Wilkie, G. J., Drozdov, A. Y., & Bortnik, J. (2022). Data-driven discovery of Fokker-Planck equation for the Earth's radiation belts electrons using physics-informed neural networks. *Journal of Geophysical Research: Space Physics*, *127*(7), e2022JA030377. https://doi.org/10.1029/2022ja030377

Chu, X., Ma, D., Bortnik, J., Tobiska, W. K., Cruz, A., Bouwer, S. D., et al. (2021). Relativistic electron model in the outer radiation belt using a neural network approach. *Space Weather*, *19*(12). https://doi.org/10.1029/2021sw002808

Daglis, I. A., Katsavrias, C., & Georgiou, M. (2019). From solar sneezing to killer electrons: Outer radiation belt response to solar eruptions. *Philosophical Transactions of the Royal Society A: Mathematical, Physical & Engineering Sciences*, *377*(2148), 20180097. https://doi.org/10.1098/rsta.2018.0097

Fälthammar, C.-G. (1965). Effects of time-dependent electric fields on geomagnetically trapped radiation. *Journal of Geophysical Research*, *70*(11), 2503–2516. https://doi.org/10.1029/jz070i011p02503

Fei, Y., Chan, A. A., Elkington, S. R., & Wiltberger, M. J. (2006). Radial diffusion and MHD particle simulations of relativistic electron transport by ULF waves in the September 1998 storm. *Journal of Geophysical Research*, *111*(A12), A12209. https://doi.org/10.1029/2005ja011211

Glauert, S. A., Horne, R. B., & Meredith, N. P. (2014). Three-dimensional electron radiation belt simulations using the BAS radiation belt model with new diffusion models for chorus, plasmaspheric hiss, and lightning-generated whistlers. *Journal of Geophysical Research: Space Physics*, *119*(1), 268–289. https://doi.org/10.1002/2013ja019281

Ioffe, S., & Szegedy, C. (2015). Batch normalization: Accelerating deep network training by reducing internal covariate shift. In F. Bach & D. Blei (Eds.), *Proceedings of the 32nd international conference on machine learning* (Vol. 37, pp. 448–456). PMLR. Retrieved from https://proceedings.mlr.press/v37/ioffe15.html

Jaynes, A. N., Ali, A. F., Elkington, S. R., Malaspina, D. M., Baker, D. N., Li, X., et al. (2018). Fast diffusion of ultrarelativistic electrons in the outer radiation belt: 17 March 2015 storm event. *Geophysical Research Letters*, *45*(20), 10874. https://doi.org/10.1029/2018gl079786

Jaynes, A. N., Li, X., Schiller, Q. G., Blum, L. W., Tu, W., Turner, D. L., et al. (2014). Evolution of relativistic outer belt electrons during an extended quiescent period. *Journal of Geophysical Research: Space Physics*, *119*(12), 9558–9566. https://doi.org/10.1002/2014ja020125

Katsavrias, C., Aminalragia-Giamini, S., Papadimitriou, C., Daglis, I. A., Sandberg, I., & Jiggens, P. (2021). Radiation belt model including semi-annual variation and solar driving (sentinel). *Space Weather*, *20*(1), e2021SW002936. https://doi.org/10.1029/2021sw002936

Katsavrias, C., Daglis, I. A., & Li, W. (2019). On the statistics of acceleration and loss of relativistic electrons in the outer radiation belt: A superposed epoch analysis. *Journal of Geophysical Research: Space Physics*, JA026569. https://doi.org/10.1029/2019ja026569

Katsavrias, C., Daglis, I. A., Li, W., Dimitrakoudis, S., Georgiou, M., Turner, D. L., & Papadimitriou, C. (2015). Combined effects of concurrent Pc5 and chorus waves on relativistic electron dynamics. *Annales Geophysicae*, *33*(9), 1173–1181. https://doi.org/10.5194/angeo-33-1173-2015

Katsavrias, C., Daglis, I. A., Turner, D. L., Sandberg, I., Papadimitriou, C., Georgiou, M., & Balasis, G. (2015). Nonstorm loss of relativistic electrons in the outer radiation belt. *Geophysical Research Letters*, *42*(24), 10521–10530. https://doi.org/10.1002/2015gl066773

Katsavrias, C., Nasi, A., Daglis, I. A., Aminalragia-Giamini, S., Dahmen, N., Papadimitriou, C., et al. (2022). The "SafeSpace" database of ULF power spectral density and radial diffusion coefficients: Dependencies and application to simulations. *Annales Geophysicae*, *40*(3), 379–393. https://doi.org/10.5194/angeo-40-379-2022

Katsavrias, C., Sandberg, I., Li, W., Podladchikova, O., Daglis, I., Papadimitriou, C., et al. (2019). Highly relativistic electron flux enhancement during the weak geomagnetic storm of April–May 2017. *Journal of Geophysical Research: Space Physics*, *124*(6), 4402–4413. https://doi.org/10.1029/2019ja026743

Kingma, D., & Ba, L. (2015). Adam: A method for stochastic optimization. In *ICLR 2015*. Retrieved from https://hdl.handle.net/11245/1.505367

Lejosne, S. (2019). Analytic expressions for radial diffusion. *Journal of Geophysical Research: Space Physics*, *124*(6), 4278–4294. https://doi.org/10.1029/2019ja026786

Lejosne, S., & Kollmann, P. (2020). Radiation belt radial diffusion at Earth and beyond. *Space Science Reviews*, *216*(1), 19. https://doi.org/10.1007/s11214-020-0642-6

Li, W., Ma, Q., Thorne, R. M., Bortnik, J., Zhang, X.-J., Li, J., et al. (2016). Radiation belt electron acceleration during the 17 March 2015 geomagnetic storm: Observations and simulations. *Journal of Geophysical Research: Space Physics*, *121*(6), 5520–5536. https://doi.org/10.1002/2016ja022400

Liu, W., Tu, W., Li, X., Sarris, T., Khotyaintsev, Y., Fu, H., et al. (2016). On the calculation of electric diffusion coefficient of radiation belt electrons with in situ electric field measurements by THEMIS. *Geophysical Research Letters*, *43*(3), 1023–1030. https://doi.org/10.1002/2015gl067398

Ma, Q., Li, W., Bortnik, J., Thorne, R. M., Chu, X., Ozeke, L. G., et al. (2018). Quantitative evaluation of radial diffusion and local acceleration processes during GEM challenge events. *Journal of Geophysical Research: Space Physics*, *123*(3), 1938–1952. https://doi.org/10.1002/2017ja025114

Ma, Q., Li, W., Thorne, R. M., Ni, B., Kletzing, C. A., Kurth, W. S., et al. (2015). Modeling inward diffusion and slow decay of energetic electrons in the Earth's outer radiation belt. *Geophysical Research Letters*, *42*(4), 987–995. https://doi.org/10.1002/2014gl062977

Ma, Q., Li, W., Thorne, R. M., Nishimura, Y., Zhang, X.-J., Reeves, G. D., et al. (2016). Simulation of energy-dependent electron diffusion processes in the Earth's outer radiation belt. *Journal of Geophysical Research: Space Physics*, *121*(5), 4217–4231. https://doi.org/10.1002/2016ja022507

Morley, S. K., Friedel, R. H. W., Spanswick, E. L., Reeves, G. D., Steinberg, J. T., Koller, J., et al. (2010). Dropouts of the outer electron radiation belt in response to solar wind stream interfaces: Global positioning system observations. *Proceedings of the Royal Society A: Mathematical, Physical & Engineering Sciences*, *466*(2123), 3329–3350. https://doi.org/10.1098/rspa.2010.0078

Nasi, A., Daglis, I., Katsavrias, C., & Li, W. (2020). Interplay of source/seed electrons and wave-particle interactions in producing relativistic electron PSD enhancements in the outer Van Allen belt. *Journal of Atmospheric and Solar-Terrestrial Physics*, *210*, 105405. https://doi.org/10.1016/j.jastp.2020.105405

Nasi, A., Katsavrias, C., Daglis, I., Sandberg, I., Aminalragia-Giamini, S., Li, W., et al. (2022). An event of extreme relativistic and ultra-relativistic electron enhancements following the arrival of consecutive corotating interaction regions: Coordinated observations by Van Allen Probes, Arase, Themis and Galileo satellites. *Frontiers in Astronomy and Space Sciences*, *9*, 949788. https://doi.org/10.3389/fspas.2022.949788

Olifer, L., Mann, I. R., Ozeke, L. G., Claudepierre, S. G., Baker, D. N., & Spence, H. E. (2021). On the similarity and repeatability of fast radiation belt loss: Role of the last closed drift shell. *Journal of Geophysical Research: Space Physics*, *126*(11), e2021JA029957. https://doi.org/10.1029/2021ja029957

Ozeke, L. G., Mann, I. R., Murphy, K. R., Rae, I. J., & Milling, D. K. (2014). Analytic expressions for ULF wave radiation belt radial diffusion coefficients. *Journal of Geophysical Research: Space Physics*, *119*(3), 1587–1605. https://doi.org/10.1002/2013ja019204

Reeves, G. D., & Daglis, I. A. (2016). Geospace magnetic storms and the Van Allen radiation belts. In *Waves, particles, and storms in geospace* (pp. 51–79). Oxford University Press. https://doi.org/10.1093/acprof:oso/9780198705246.003.0004

Samara, E., Pinto, R. F., Magdalenić, J., Wijsen, N., Jerčić, V., Scolini, C., et al. (2021). Implementing the MULTI-VP coronal model in EUHFORIA: Test case results and comparisons with the WSA coronal model. *Astronomy &amp Astrophysics*, *648*, A35. https://doi.org/10.1051/0004-6361/202039325

Sandhu, J. K., Rae, I. J., Wygant, J. R., Breneman, A. W., Tian, S., Watt, C. E. J., et al. (2021). ULF wave driven radial diffusion during geomagnetic storms: A statistical analysis of Van Allen probes observations. *Journal of Geophysical Research: Space Physics*, *126*(4). https://doi.org/10.1029/2020ja029024

Sarma, R., Chandorkar, M., Zhelavskaya, I., Shprits, Y., Drozdov, A., & Camporeale, E. (2020). Bayesian inference of quasi-linear radial diffusion parameters using Van Allen probes. *Journal of Geophysical Research: Space Physics*, *125*(5), e2019JA027618. https://doi.org/10.1029/2019ja027618

Shprits, Y. Y., Allison, H. J., Wang, D., Drozdov, A., Szabo-Roberts, M., Zhelavskaya, I., & Vasile, R. (2022). A new population of ultra-relativistic electrons in the outer radiation zone. *Journal of Geophysical Research: Space Physics*, *127*(5), e2021JA030214. https://doi.org/10.1029/2021ja030214

Smirnov, A. G., Berrendorf, M., Shprits, Y. Y., Kronberg, E. A., Allison, H. J., Aseev, N. A., et al. (2020). Medium energy electron flux in Earth's outer radiation belt (MERLIN): A machine learning model. *Space Weather*, *18*(11), e2020SW002532. https://doi.org/10.1029/2020sw002532

Subbotin, D. A., & Shprits, Y. Y. (2009). Three-dimensional modeling of the radiation belts using the versatile electron radiation belt (VERB) code. *Space Weather*, *7*(10), W000452. https://doi.org/10.1029/2008sw000452

Thanasoula, K., Katsavrias, C., Nasi, A., Daglis, I. A., Balasis, G., & Sarris, T. (2022). Magnetospheric ULF wave dependence on interplanetary coronal mass ejections and stream interaction regions. https://doi.org/10.5194/egusphere-egu22-475

Tu, W., Elkington, S. R., Li, X., Liu, W., & Bonnell, J. (2012). Quantifying radial diffusion coefficients of radiation belt electrons based on global MHD simulation and spacecraft measurements. *Journal of Geophysical Research*, *117*(A10), 10210. https://doi.org/10.1029/2012ja017901

Turner, D. L., Shprits, Y., Hartinger, M., & Angelopoulos, V. (2012). Explaining sudden losses of outer radiation belt electrons during geomagnetic storms. *Nature Physics*, *8*(3), 208–212. https://doi.org/10.1038/nphys2185

Varotsou, A., Boscher, D., Bourdarie, S., Horne, R. B., Glauert, S. A., & Meredith, N. P. (2005). Simulation of the outer radiation belt electrons near geosynchronous orbit including both radial diffusion and resonant interaction with whistler-mode chorus waves. *Geophysical Research Letters*, *32*(19), L19106. https://doi.org/10.1029/2005gl023282

Varotsou, A., Boscher, D., Bourdarie, S., Horne, R. B., Meredith, N. P., Glauert, S. A., & Friedel, R. H. (2008). Three-dimensional test simulations of the outer radiation belt electron dynamics including electron-chorus resonant interactions. *Journal of Geophysical Research*, *113*(A12), A05216. https://doi.org/10.1029/2007ja012862